# In Situ Optical Investigations of Lithium Depositions on Pristine and Aged Lithium Metal Electrodes

Hannes Kühnle<sup>1</sup>, Edwin Knobbe<sup>2</sup>, Egbert Figgemeier<sup>1,3,4,z</sup>

- <sup>2</sup> BMW Group, Battery Cell Competence Centre, 80788, Munich, Germany
- <sup>3</sup> Juelich Aachen Research Alliance, JARA-Energy, 52425, Jülich, Germany
- <sup>4</sup> Helmholtz Institute Münster (HI MS), IEK-12, Forschungszentrum Jülich, 52066, Aachen, Germany

<sup>z</sup>Email: <u>e.figgemeier@fz-juelich.de</u>

#### Abstract

A custom-designed in situ optical cell is used to investigate the behavior of lithium (Li<sup>0</sup>) deposition in a symmetrical face-to-face setup. The experiment aims at monitoring the lithium deposition on both pristine and aged lithium foils, as a function of the waiting time between the lithium electrodes and the electrolyte (LP30: 1.0 M LiPF<sub>6</sub> in EC: DMC (50/50) (v/v))). Constant current and electrochemical impedance spectroscopy measurements are applied at ~28 °C. The experiments show that lithium metal deposits in a wide range of morphologies, which are cataloged in terms of forms, structures, textures and colors for better visualization and improved analysis. Pristine lithium electrodes show tree-like deposition morphologies over the entire range of applied waiting times, but aged samples provided fibrous, and spheroidal forms as dominant lithium deposition morphologies at waiting times ≥ 24 hours. Gas-treated metal foils (artificially aged by exposing pristine lithium to N<sub>2</sub> at 25 °C for 1 hour) showed a similar deposition behavior as the aged-overtime foils. The storage of lithium has a measurable influence on the deposition behavior on lithium foils. The obtained results help to further understand the lithium deposition behavior under different realistic conditions, which is for instance applicable to rechargeable lithium metal batteries.

<sup>&</sup>lt;sup>1</sup> Institute for Power Electronics and Electrical Drives (ISEA), RWTH Aachen University, 52066, Aachen, Germany

# Introduction

In the last 150 years the effective energy density of rechargeable batteries increased from 40 Wh kg<sup>-1</sup> for lead-acid batteries to about ~250 Wh kg<sup>-1</sup> for state-of-the-art lithium-ion batteries (LIB). Attempts to go beyond the horizon of the prevailing LIBs requires the introduction of new chemistries.<sup>1</sup> In the road for high-energy and reliable Next-Generation batteries, the rechargeable lithium metal battery (LMB) is considered as one of the most promising battery technologies with a great potential to increase the energy density. The outstanding properties, such as the extremely high theoretical capacity (3860 mAh g<sup>-1</sup>)<sup>2</sup>, the very low negative redox potential (-3.040 V vs. SHE)<sup>2-4</sup> and the low atomic weight ([6.938 u, 6.997 u])<sup>5</sup>, are among the beneficial features hailing lithium (Li<sup>0</sup>) as a "holy grail" electrode. However, despite all its advantages, there are various obstacles that hinder the practical large-scale commercialization of LMBs. Lithium metal reacts continuously with the electrolyte due to its high reactivity, which leads to electrolyte depletion and forms deposition products on the electrode surface. Furthermore, lithium leads to the growth of sharp and spiky lithium depositions, called dendrites, on its surfaces. This results in low Coulombic and energy efficiencies and can lead to short-circuits, which are a safety-induced risk.<sup>8–12</sup>

To exploit the advantages of lithium metal anodes by evading the above-mentioned hurdles, the scientific community has been engaged in exploring various mitigating strategies, and applying characterization techniques aiming at understanding the behavior of lithium deposition/stripping and the nature and behavior of the various lithium deposition morphologies. Numerous groups have recently attempted to better monitor and understand the behavior of lithium deposition by using various in situ analytical techniques, which include in situ X-ray photoelectron spectroscopy (XPS)<sup>13</sup>, in situ Auger electron spectroscopy (AES/AEM)<sup>14</sup>, in situ scanning electron microscopy (SEM)<sup>15–17</sup>, in situ transmission electron microscopy (TEM)<sup>18,19</sup>, in situ atomic force microscopy (AFM)<sup>20</sup> as well as in situ optical cells<sup>21–34</sup>.

Despite these global research efforts, the behavior of lithium deposition is still elusive and demands further in-depth investigations. This work investigates the electrochemical deposition characteristics and patterns of pristine and aged lithium metal electrodes as a function of the contact time between the metal surface and the electrolyte solution. Furthermore, we evaluate our working hypothesis, that nitrogen plays an important role in surface interactions on lithium metal foils with the surrounding atmosphere. Therefore, a custom-designed face-to-face in situ optical cell was designed to conduct real time studies with a digital microscope of various phenomena of lithium deposition during a constant current (CC) phase. Electrochemical impedance spectroscopy (EIS) measurements were recorded before, during and after a CC-phase. The obtained visual recordings of the lithium depositions were catalogued according to their morphology, texture and color. The results highlight further insights into the understanding of the lithium deposition behavior under various defined conditions.

# **Experimental**

# **Investigated materials/samples**

Three different types of lithium foils were investigated. First, a pristine lithium foil by Albemarle Corporation, referred to as **Li-PRISTINE**. Secondly, Li-ARTIFICIALLY-

AGED (which will be abbreviated as **LI-ART.-AGED**), prepared by exposing Li-PRISTINE to nitrogen gas (N<sub>2</sub>) for 1 h at 25 °C in the evacuation chamber of a glove box (both sides of the foil). Therefore, the lithium foil was transferred from the argon (Ar) gas-filled glovebox into the Ar-filled evacuation port of the glove box. Vacuum (Leybold Trivac D16B,  $\leq 2 \times 10^{-3}$  mbar) was applied and N<sub>2</sub> was injected. The lithium samples stayed inside the evacuation port for 1 h, before the port was five times evacuated and refilled with Ar. Thirdly, a pristine lithium foil provided by Rockwood Lithium Inc., which is referred to as **Li-TIME-AGED**. This Li-TIME-AGED material was stored for several years in an Ar-filled glovebox, it is ascribed as "aged-over-time". All three lithium samples were immediately transferred and kept in Ar-filled gloveboxes, which were connected to a N<sub>2</sub>-removel unit. The electrolyte used throughout the whole study was LP30 (1.0 M LiPF<sub>6</sub> in EC: DMC (50/50 (v/v), battery grade), obtained from Sigma-Aldrich.

#### **Experimental setup**

We developed a custom-made optical electrochemical cell-setup to investigate the characteristics of lithium depositions on lithium metal electrodes. The optical cell consists of two modules. The first module M1 (Figure 1, green, shaded) is a gastight transport container, which was designed to keep the Ar-atmosphere inside and the ambient air and moisture outside. The container is equipped with connector pins, a gasket and a lid with an optical sapphire glass window. The optical window provides a direct view into the interior of the box on the targeted electrode surface. The M1-box was milled from a single polyetheretherketone (PEEK) block. Stainless steel connections (SSTL 1.4404) have been integrated to connect a second module with external devices, e.g. a potentiostat. The M1-lid was milled from a separate PEEK-block. An optical window (sapphire glass) was integrated and sealed with a gasket. By placing a custom made gasket between the M1-box and the M1-lid, the system was sealed gas-tight and protected against contamination by moisture (H<sub>2</sub>O) and atmospheric gases (O<sub>2</sub>, N<sub>2</sub>, etc.).

A second Module M2 (core unit) (Figure 1, magenta, bright) contains the electrodes and the electrolyte, is located in the center of M1 and can be seen as the "actual cell". It is built-up from milled PEEK-cuboids. Where required, cutouts were milled into the blocks to enable the integration of smaller parts, such as current collectors made from stainless steel (SSTL, 1.4404), cable connections (SSTL, 1.4404) and temperature sensors (NTC thermoresistor TDK / Epcos B57703M0103, 10 K, 3988K, 2 %). The core unit is built-up by three subgroups: (1) outer spacers with threads and cutouts for screws to fasten the various PEEK-parts together, (2) electrode holders containing the current collectors and cable connections, and (3) an inner spacer-block serving as an electrolyte reservoir and for fixing the lithium electrodes on their designed positions on the current collectors.

Before assembling the optical cell, the modules M1 and M2 were first dried under vacuum at 40 °C for 24 h and were then transferred into an Ar-filled glovebox. The lithium foils were mounted on the current collectors, while the parts of the modules were still separated. After the lithium electrodes were attached, the individual module parts (M2) and gaskets (FPM) were joined and a torque of 3.7 Nm was applied. The current collectors were in the assembled state orientated face-to-face and each equipped with a temperature sensor. The surfaces of the lithium electrodes, which were not covered by the inner spacer, were referred to as accessible active lithium. The accessible electrode surface for a single electrode was 13.08 cm² and provided the basis for calculating the current density of 1.00 mA cm². The distance between the two pristine lithium electrode surfaces was

8.4 mm. No separator was installed, because the electrode surfaces were not in direct contact with each other.

In the next step, the core-unit module M2 was put into the transport container module M1. Once all cable connections inside the optical cell were wired, 20 mL LP30 electrolyte was filled into the electrolyte reservoir (M2, inner spacer). This moment was referred to as t<sub>zero</sub> (TABLE I). For each experiment t<sub>zero</sub> was used to monitor the contact time between the lithium metal and the electrolyte. A custom-designed gas-tight gasket was placed on the edge of the reservoir to function as a second barrier against contamination by moisture and atmospheric gases and to prevent evaporation of the volatile components (i.e., DMC) of the electrolyte. Evaporation of electrolyte would change the electrolyte composition and bulk properties such as viscosity, conductivity, etc., thus impacting the performance. The M1-lid with the optical window was mounted on top of the M1-box and the whole assembly was sealed gastight. The fully assembled optical cell was then transferred out of the glovebox into the laboratory atmosphere to perform the combined optical and electrochemical experiments.

The optical cell was then positioned under a digital microscope (KEYENCE VHX-6000) and the connector pins were connected in a two-electrode-setup (working electrode (WE) vs. a combined counter (CE) and reference electrode (RE)) to a potentiostat (Zahner ZENNIUM). The temperature sensors inside the optical cell were connected to a PID-controller (OsTech PC-OS11-t85-683) using it as a thermometer. The electrochemical experiments were performed at room temperature (RT) in an air-conditioned laboratory (approx. 25 °C). Due to the applied light sources (HLQ3, HETHIS), which emit a low but constant heat radiation, approximately 28 °C was measured on both electrode sides during all experiments.

For further optical characterization, a Keyence laser microscope (KEYENCE VK-9700) was used to record the surfaces of the lithium foils at 100x magnification.

# **Experimental procedure**

In the first part of the study, we made in situ records of lithium deposition processes taking place on lithium metal electrode surfaces during the electrochemical test protocols.

It has to be noted, that the surface layers of commercial, "pristine" lithium metal foils are covered with an inorganic "native" passivation layer. Pure lithium metal surfaces are very sticky and difficult to process. This is why lithium metal suppliers handle it under dry room conditions in the presence of O<sub>2</sub>, N<sub>2</sub>, ppm traces of H<sub>2</sub>O, and so forth, to form a non-sticky and processable surface layer. It has to be underlined that lithium metal is only in theory deposited on pure lithium metal surfaces, but the deposition takes in reality place on a thin ceramic layer consisting of e.g. lithium oxide (Li<sub>2</sub>O), lithium carbonate (Li<sub>2</sub>CO<sub>3</sub>) or hydroxides (LiOH). This notice is supported by Wu et al.<sup>35</sup>, where the authors obtained similar results during XPS measurements on "Li as received" samples.

Every time a newly assembled optical cell was placed under the digital microscope, the same buffer time of 900 s (TABLE I) was employed for all experiments to transfer and set up the optical cell in the measurement setup. To study lithium metal depositions as a function of the contact time between the electrode and the electrolyte, the same test protocol with different initial waiting times was carried out: 3 h, 8 h, 24 h and 48 h. This initial waiting time was always before the first EIS measurements (500 kHz - 10 mHz) and the CC-phase, as can be seen in TABLE I.

During the different stages of each individual experiment images were recorded in distinctive ways. In the first stage, under open circuit conditions (TABLE I, buffer time

plus corresponding WAIT 1-phase A, B, C or D), photos of both electrode surfaces were taken at angles of  $0^{\circ}$ ,  $5^{\circ}$  and  $20^{\circ}$  and magnifications of 5x, 20x and 50x (VH-Z 00T VH zoom lens 5x - 50x).

The first EIS measurement (EIS 1) started after both the buffer time and the corresponding waiting time had elapsed.

In the second stage, the lithium deposition process on the negative electrode was recorded during the CC-phase with a current density of  $j = 1.00 \text{ mA cm}^{-2}$ . A self-timer in the digital microscope took every 120 seconds images of the lithium metal deposition at an angle of  $5^{\circ}$  and a 5x magnification (VH-Z00T VH zoom lens 5x).

The measurement protocol stopped after the fourth EIS measurement (EIS 4) was completed. This marked the start of the third stage and images were taken from both electrode sides (deposition, pitting) at angles of  $0^{\circ}$ ,  $5^{\circ}$  and  $20^{\circ}$  and with magnifications between 5x and 500x (VH-Z00T VH zoom lens 0x-50x, VH-Z50T VH zoom lens 50x-500x).

#### **Results and Discussion**

# **Optical results**

First, we looked at the obtained lithium deposition characteristics from a macroscopic point of view (magnification  $\leq 50x$ ), which was followed by the evaluation of the individual lithium crystallites from a microscopic perspective (magnification  $\geq 50x$ ). On the macroscopic scale, the recorded structures of lithium metal depositions showed similar textures under the same experimental setup conditions and were thus meaningfully comparable.

In order to catalog the observed lithium structures, the morphologies were classified in four super classes and twelve subclasses. The four super classes were classified as: "tree-like" (Figure 4, Type A), "spherical" (Figure 4, Type B), "planar" (Figure 4, Type C) and "spiky" (Figure 4, Type D) morphologies.

The first superclass, referred to as "tree-like", is the most frequently appearing deposition type in optical cell setups (gap between electrodes) at RT.<sup>24,25,27,33,34</sup> Brissot et al. introduced terminologies such as "tree-like"<sup>36</sup> and "arborescent like"<sup>37</sup> to describe such morphologies. The tree-like representatives form voluminous structures with irregularly and protruding patterns that resemble branches of tree crowns. The full structure is built up from small, compact and knobby basic building blocks, which result in a rough and uneven surface texture. During a CC-phase, the individual branches grow outwards from the center of the structure. The individual branches interlock with each other and form voluminous but compact structures. Superclass type B summarizes all subclasses that show spherical deposition patterns. Love et al. identified curved lithium deposition structures at -10 °C in a LP30 electrolyte and attributed them as "mushroom-like" and "rounded dendrites".<sup>27</sup> However, to better summarize the entirety of the identified subclasses, the term "spherical" is chosen for this superclass.

Planar<sup>38</sup> structures are identified as the third superclass. These deposition representatives do not form large voluminous structures as in the first two-super class types. The lithium metal deposits are found to be evenly distributed instead of forming a very local three-dimensional, voluminous structures. The fourth superclass is referred to as "spiky". In

general, all representatives of this lithium deposition super class showed fine, longitudinal and often pointed shapes.

The shape and patterns of the lithium deposition morphologies play a crucial role in the determination of the electrochemical and safety performance of LMBs. Among all observed morphologies, tree-like and spiky like-structures could be treated as more severe dendritic, thus worsening the lithium deposition/stripping efficiency and increasing safety-induced risks.

Furthermore, twelve subclasses are identified as can be seen in Figure 5, which in turn are assigned to the corresponding super classes. The subclasses "elliptical tree" and "bulky tree" are assigned to the superclass "tree-like" and are the most common structures obtained in this study. The elliptical tree type (Figure 5a) grew more in length than in width (length:width ratio of about 2:1). In contrast, the bulky tree type (Figure 5b) expanded quite evenly in all directions during the lithium deposition as evidenced by the length to width ratio of ca. 1:1. For all three lithium types (Li-PRISTINE, Li-ART.-AGED, Li-TIME-AGED), the waiting period between 3 h and 8 h led to the formation of tree-like morphologies. For Li-Pristine, this trend continued towards higher waiting times of 24 h and 48 h.

The "spherical" superclass is divided into four subclass types, which are called "sea ball", "steel wool", "nugget" and "crumb" (see Figure 5c, d, e and f respectively). Spherical structures are the predominant type of lithium deposition patterns for waiting times  $\geq 24$  h for samples from the Li-ART.-AGED and Li-TIME-AGED foils. However, in the complete range of waiting times of 3 h, 8 h, 24 h and 48 h no spherical structures could be found in the case of Li-PRISTINE foils.

The first subclass in the second superclass ("spherical") presents isolated and stand-alone spherical structures. These crystallites are referred to as "sea balls" (Figure 5c), since they appeared similar to the fibrous marine materials one can find at the seashore. The surface textures did not show the knobby appearance of the tree-like structures. In contrast, fluffy networks of thousands of filigree and fibrous elements are observed. A more frequent phenomenon than the individual sea ball structures were agglomerations of sea balls connected by a network of lithium fibers. This structure is referred as "steel wool" (Figure 5d). The third subclass "nugget" (Figure 5e) is found to have a solid, shiny, and drop-like structure. The shiny surface differ from the regular grey-matt appearance, because most lithium structures showed and appeared to be deposited as a solid piece of lithium metal (Li<sup>0</sup>). The fourth subclass within the spherical superclass is named as "crumb" (Figure 5f). This structure type combines the fluffy, and fibrous steel wool type as a basic building block upon which the tree-like solid lithium depositions crystallize to form small agglomerates.

The third superclass, characterized as "planar", contains four characteristic patterns enlisting "uniform", "lamellar", "blank" and "pitting". Of these subclasses, only the "uniform" (Figure 5g) and "lamellar" (Figure 5h) type properly describe the actual lithium deposition behavior. The uniform-type describes lithium, which is homogeneously deposited on the electrode surface and covered a certain electrode area uniformly with tiny lithium crystallites. The lamellar-type is also deposited as tiny lithium crystals, but as its name implies, the characteristic patterns showed parallel oriented straight lines. The origin for this lamellar deposition behavior probably results from the original mechanical deformation at the lithium surface, which are barely visible to the naked eye. We assumed that these existing grooves might have been introduced in the lithium foil during the

manufacturing process. A third subclass is named as "blank" (Figure 5i). During the lithium deposition process of the CC-phase, some regions on the electrode surface remained untouched/pristine and look like the initial state. As it is difficult to show this pattern, some other lithium deposition structures were intentionally not cropped in the image, to emphasize the untouched state of the corresponding electrode surface.

This phenomenon could be explained by the presence of areas without lithium depositions next to areas with deposited lithium structures. The lithium depositions (elevations on the electrode) provide higher local electric fields compared to the flat surrounding areas<sup>39</sup>. Thus, the individual protruding branches and tips of the bulky structures affect the incoming lithium-ions much more and lithium metal is more-likely deposited on preexisting structures rather than forming new crystallites. This process is self-enhancing, as protruding structures continue to further grow and thus their electric field further increases<sup>39–41</sup>. For completeness of all observed planar lithium natural phenomena, the fourth representative of the planar super class is identified as "pitting" (Figure 5j). <sup>33,42–44</sup> Although pitting (formation of crater-shaped pits on the electrode surface due to dissolution of active material caused by an applied voltage) is the opposite of lithium deposition, it is defined as a planar structure. The pitting effect could be identified at the opposite electrode with the optical cell structure presented in this study.

The fourth and last super class is described as "spiky" and grouped filigree elongated and often-pointed lithium deposition structures. The first representative of this superclass is called the "thorn" type (Figure 5k). The representatives of this subclass are shaped like the thorn of a plant, which is broader in the lower part and tapers towards the tip. A large number of differently dimensioned structures have been found, ranging from a few hundredths of a millimeter up to structures of millimeter size. The second subclass type is referred to as "whisker" (Figure 5l). 32,45,46 Whiskers can be described as filamentous, fiberlike lithium structures or as "fibrous crystals" with a constant diameter. Yamaki et al. reported, that lithium whiskers grow mainly from the base. 45

In the next section, the focus is on the surface properties/textures and color appearances of the lithium structures (see Figure 6). Four texture types were identified: "solid & smooth", compact & rough", "fibrous & fluffy" and "fibrous & chunky". The "solid & smooth" texture (Figure 6a) corresponds to spherical nugget-type as well as to the planar empty-type. The surface of these lithium morphologies is even and homogeneous and does not show any fibers or knobs on it. The "compact & rough" (Figure 6b) texture could be assigned to all tree-like types, partly to the spherical crumb-type as well as to the planar uniform- and lamellar types. The surface of this texture is rough and is build up from knobby-like particles.

The "fibrous & fluffy" texture (Figure 6c) could be assigned to the spherical sea-ball and steel wool types as well as partly to the crumb-type. The surface property consists of a web / network consisting of the individual thread-like structures ("whiskers"). The "fibrous & chunky" texture (Figure 6d) could be assigned to the crumb-type, where the surface property consists of a web / network consisting of individual thread-like structures and is additionally studded with solid knobby particles.

Furthermore, extraordinary color phenomena have been found and are cataloged further. In contrast to the standard appearance of lithium depositions, with its range of matt shades of gray, very rarely but regularly recurring, colored appearances were spotted. The extraordinary color appearances were referred to as "metallic", "bluish" and "orange".

The origin for the shiny surface property of the metallic-type (Figure 6e) could be attributed to a solid lithium metal surface on which the incident light is reflected due to the electron gas present in the metallic state<sup>47</sup>. The bluish (Figure 6f) and orange ("red-brown") (Figure 6g) appearances of the lithium depositions were already described by Sörgel<sup>48</sup>, who attributed the origin of the two colors to the nanostructured surface morphologies present on the electrodeposited lithium.

To complete the optical part, Figure 7 shows laser microscope images with 100x magnification, recorded from the various lithium metal foils (Li-PRISTINE, Li-ART.-AGED and Li-TIME-AGED). Li-PRISTINE (Figure 7a) shows a flawless surface with a lamellar pattern resulting from the lithium handling during production. Contours of existing fissure-like patterns on the surface can hardly be seen with a naked eye. In contrast to that, the fissure-like patterns are dominant for Li-ART.-AGED (Figure 7b) and Li-TIME AGED (Figure 7c). Even if the lamellar patterns from production are still visible, sharp and distinctive structures on the foil surface are dominant on the aged lithium foils samples. This indicates that both foil surfaces must be in a different chemical state than the original Li-PRISTINE foil. The aged lithium foils must have reacted with the surrounding atmosphere in the past, resulting in a modification of the surface.

In situ observations showed that the voluminous tree-like and spherical structures grow up to a certain point perpendicular to the electrode surface. As it is tried to extract the lithium structures by carefully removing the electrolyte, they partly collapsed under their own weight and changed their morphology. Post-mortem investigations of the crystallites in a higher resolution scanning electron microscope were not possible, because the remaining structures were covered with a salt layer as the volatile components of the electrolyte were evaporated. Attempts to wash, and thereby remove the salt layer, with dry DMC resulted in destruction of the lithium structures.

Figure 8 (a - c) shows in situ images taken during one CC-phase at three different time steps. At the first time step larger lithium crystallites have already been deposited on the lithium electrode surface (Figure 8a). With increasing duration of the CC-phase, lithium crystallites continue to grow perpendicular to the electrode surface. However, some structures (e.g. in the red circle) experienced a laterally directed force during the growth process and bend (Figure 8b). This bending could eventually even lead to the structure tearing off, which finally causes it to float to the electrolyte surface due to the small density (Figure 8c).

These observations indicate, that the growth of the voluminous tree-like and spherical structures are particularly affected by the difference in the density between the lithium foil  $(\rho_{Li} = 0.534 \text{ g cm}^{-3})^2$  and electrolyte solution  $(\rho_{LP30} = 1.30 \text{ g cm}^{-3})$ . The red dot (Figure 8a) indicates one tip in the lithium structure, which is pointing out perpendicular to the electrode surface. Depending on the nature of the lithium structure, such as volume and quality of connection points on the electrode surface, the labeled structure was bend sideward (Figure 8b). We assume that the presence of a continuous buoyancy force (See Figure 8, orange arrow) in combination with the growth of the lithium deposition during the CC-phase is the driving force. A yellow curved arrow indicates the change in the direction of the corresponding tip (position of the red dot changed). The growing process continued as long as the structure remained electrically contacted to the electrode surface. If the connection point could not handle the mechanical deformation (bend), the structure ripped off and floated to the electrolyte surface (Figure 8c).

#### **Electrochemical results**

Electrochemical measurements (500 kHz – 10 mHz) were conducted and the results are evaluated. The focus of the measurements was set on monitoring the impedances of the tested systems. Figure 9 displays four representative EIS-spectra (Nyquist plots) recorded for the Li-TIME-AGED sample during the 8hWAIT-test protocol (see also TABLE I). It was of particular interest to assess whether the impedance values showed certain trends depending on (1) the time at which the EIS-measurement were performed during the electrochemical test protocol (See EIS 1, EIS 2, EIS 3, EIS 4), (2) the waiting time (buffer time + WAIT 1), over which the electrolyte and lithium electrode were in contact and (3) the type of applied lithium foil (e.g. Li-PRISTINE. Li-ART.-AGED, Li-TIME-AGED).

Figure 9 shows an example of Nyquist-plots of the recorded EIS-spectra of a single Li-TIME-AGED 8hWAIT measurement. Due to the symmetrical cell setup, the measured impedance spectrum is the product of two Li||LP30 interfaces. In this example, the data was recorded after a defined waiting time of 8 h (WAIT 1) has passed. No CC was applied before the EIS 1 measurement was completed. The first EIS measurement (EIS 1, black squares) has the largest semicircle diameter and therefore the highest impedance of all four indicated spectra. The second EIS measurement (EIS 2, red triangles) was conducted immediately after the CC-phase was completed. Its semicircle diameter is way smaller than the EIS 1 measurement. After the EIS-2 measurement was completed, two waiting times of 3600 s followed, each coupled with one subsequent EIS measurement. For the EIS measurements EIS 3 and EIS 4 an increase of the semicircle diameters could be observed. The increase can be seen between the EIS 2 (red triangles) and the EIS 3 (green circles) measurement as well as between the EIS 3 (green circles) and the EIS 4 (blue stars) measurement. The change of the impedance spectra can also be seen by the changing position of the data point, which corresponds to the measurement at 207 Hz (See Figure 9).

To get a better insight of the scattering between the individual samples of a setup type, multiple measurements (multi-measurement, 5 - 7 times) were carried out for defined setup types (Li-PRISTINE-3h, Li-PRISTINE-8h, Li-ART.-AGED-8h, Li-TIME-AGED-8h and Li-TIME-AGED-24h). The remaining setup types were carried out as a single experiments. In summary, the overall picture for the EIS measurements can be summarized as follows: After the initial waiting times expired, the first EIS-measurements "EIS 1" were carried out. For the single-measurement setup types, one single corresponding semicircle was obtained. For the multi-measurement setup types, multiple EIS 1-spectra with varying semicircle diameters were recorded. Next, the CC-phase was carried out. Immediately after the CC-phase, the second EIS-measurement "EIS 2" was initiated. For the singlemeasurement setup types, the individual EIS 2-spectra were shifted towards smaller impedances. The same effect was observed for the multi-measurement setup types. However, in addition, the scattering between the various semicircle diameters was reduced significantly and the measured spectra (EIS 2) were then located in the same area. Next, the EIS-spectra "EIS 3" and "EIS 4" were recorded. As a result of the 1-h-waiting times between EIS 2 and EIS 3 and EIS 3 and EIS 4, the semicircle diameters of all setup types (single/multi) generally speaking increased. This trend of initially shrinking and subsequently increasing semicircle diameters was observed in all recorded experiments without exception (Li-PRISTINE, Li-ART.-AGED, Li-TIME-AGED).

To further identify and quantify trends in these impedance spectra, the measured impedance spectra were fitted using the Witzenhausen FittingGUI<sup>49</sup>. The fitting was based on data points of the semicircle (high and mid frequency area, 500 kHz - 4 Hz). The tail (low frequency area, 4 Hz - 10 mHz) was not taken into account for the fitting process. Figure 10 shows the electric equivalent circuit model (EEC), which consists of a serial connection of a resistor ( $R_{ser}$ ) and two ZARC-elements (ZARC,1 and ZARC,2), that is applied to fit the dominant semicircle. The "tails" of the impedance spectra with the lower frequency area were not taken into account for the fitting.

Figure 11 shows the fitted data for the resistance of the second ZARC-element ( $R_{ZARC,2}$ ). For reasons of clarity, we have plotted only the arithmetic mean value of the fits from the multi-measurements, indicated by neon shades. It is subdivided into spectra according to the respective initial waiting times (WAIT 1): 3 h (Figure 11a), 8 h (Figure 11b), 24 h (Figure 11c), 48 h (Figure 11d). The y-axis show the calculated resistances of the ZARC,2-element in ohm. The x-axis show the number of the EIS-measurements performed during the test protocol.

The fitted values of the first EIS spectra (EIS 1) were found to be in general higher in comparison to the subsequent values. Similar to the experimentally determined EIS semicircles, a trend of first shrinking and then increasing ZARC,2 resistances with increasing EIS number could also be observed for the ZARC,2 resistances. However, the deviations in some series of fitted data points are too large challenging the identification of trends.

Looking only at the first x-data point in Figure 11, EIS-No. 1, the sample Li-PRISTINE (red) shows the lowest resistance values for all four waiting times (3 h, 8 h, 24 h, 48 h) among the tested lithium foils. The second highest resistance values can be found for Li-TIME-AGED (blue), which is then followed by Li-ART.-AGED (green) with the highest resistance values at EIS-No. 1.

# Comparison and interpretation of results.

TABLE III summarizes the obtained data from the above sections. Three different types of lithium foils were investigated, namely Li-PRISTINE, Li-ART.-AGED and Li-TIME-AGED. The recorded images of the lithium depositions from the optical in situ cell setup revealed different types of morphologies (see Figure 5). Considering the large variety of obtained morphologies, it is difficult to generally address the lithium depositions as "dendrites".

The optical data of various samples indicate that the morphology of the depositions seem to depend mainly on two factors, (1) on the surface condition of lithium samples and (2) the way lithium samples have been stored/treated (pristine, N<sub>2</sub>-treated, stored for a long time). The results from the laser microscope investigations (Figure 7) suggest that the surface character of aged lithium samples differs from that of pristine lithium samples. It is therefore plausibly inferred that aged lithium samples show a similar deposition behavior, but it is different in comparison to the pristine samples. For pristine lithium, no spherical morphologies could be identified in the full range of tested intervals. However, for aged lithium samples spherical morphologies were observed for waiting times equal or above 24 h. This means that, although lithium metal is stored under presumably ideal

conditions in an Ar-filled glove box, trace amounts of moisture (H<sub>2</sub>O) and atmospheric gases (O<sub>2</sub>, N<sub>2</sub>, etc.) will alter the surface properties of the lithium metal foils over time.

The contact time between electrolyte (LP30) and lithium metal seems to have an influence on the evolution of deposition morphologies. This can be seen for the aged samples, where for shorter waiting times (3hWAIT and 8hWAIT) tree-like structures were observed as predominant morphologies, while at higher waiting times (24hWAIT and 48hWAIT), spherical ones started to emerge.

In order to provide reliable remarks on the possibly different influences of the lithium morphologies on the performance and safety of lithium metal based cells, further experiments and tests utilizing different analytical tools are required. With our preliminary results, one can state that handling of lithium films under different conditions leads to different lithium deposition morphologies, ranging from fibrous and fluffy properties, as found in sea ball structures, to compact and rough properties, as found in tree-like structures (see Figure 6). While the compact structures tend to form knobby, rough structures, many small fibrous whisker-like structures can be found in the fluffy structures. In LMBs, these fine structures could theoretically find their way through the porous separator and thus pose a potential safety risk.

With regard to the interpretation of the EIS data, one can see that the first EIS measurement (EIS 1) generally represents one of the largest semicircle diameters of each setup type and thus one of the highest ZARC,2 values of the four EIS-spectra (see TABLE IV).

The high impedance values of the EIS-No. 1 may be attributed to a less conductive native film on the lithium metal foil as obtained by the manufacturer in combination with the passivation film formed while the lithium metal is in contact with the electrolyte at open circuit voltage. Immediately after the subsequent CC-phase was completed, the second EIS measurement (EIS 2, red triangles) was conducted. The measured results showed that the diameter of the EIS 2 semicircles decreased significantly compared to the EIS 1 measurements. We assume that lithium metal structures have grown from the top of the lithium surface through the passivation layers into the electrolyte. This would have generated a new and fresh lithium surfaces. The newly formed lithium metal structures could be thus covered with a thinner layer of decomposition products compared to the electrode state during the EIS 1 measurement, which results in a lower impedance for the EIS 2 measurement. EIS 3 and EIS 4) could be explained with the growth of a layer of decomposition products, e.g. from a decomposition of electrolyte (LP30) and reactive electrode surface (lithium metal) leading to a more resistive interphase. 50,51

# Comment on the bold, underlined and blue values in TABLE IV:

The Nyquist plots of the EIS raw data (see. exemplarily Figure 9) on which the fitting data in Table IV is based all show the same trend: EIS 1 (large semicircle), EIS 2 (semicircle becomes small), EIS 3 (semicircle becomes larger), EIS 4 (semicircle becomes larger). The Nyquist plots (sets of EIS raw data) were read in and processed using the Witzenhausen FittingGUI, yielding the fitting data in TABLE IV. The FittingGUI is designed in a way that virtual data points based on a fitting-model can be fitted to the original data points. By varying the input parameters so that the superposition of the output parameters matches the original data as closely as possible, the FittingGUI aims to keep the deviation between the virtual and the measured data points as small as possible. In this study, the applied model is mainly based on two ZARC elements resulting in a superposition of two semicircles.

Generally, the resulting virtual fitting curve was best fitted by using a smaller ZARC,1 semicircle and a larger ZARC,2 semicircle. However, for the above-mentioned outlier fitting data points, the size ratio for an optimal fitting of the virtual data points on the measured data points was inverse, which probably led to a deviation from the general trend.

Our group approached this publication under the following assumption: Lithium metal deposition depends on the history of the applied lithium metal foil (electrode). According to our hypothesis different storage conditions have an influence on the character of the lithium metal electrode surfaces and thus a direct impact on the structure, morphology and texture of the lithium deposition. The various analyses of the differently stored/treated lithium foils in a symmetrical Li<sup>0</sup>||Li<sup>0</sup> setup (gap between the electrodes, no direct contact) allowed to observe trends within the series of tests. Combining the obtained data of the three different types of lithium foils leads to the following conclusions:

**Li-PRISTINE**, the lithium foil obtained from the manufacturer has not received any further treatment and was used directly in its original state for the investigations. The laser microscopic images show a flawless surface with a lamellar pattern resulting from the lithium handling during production. Furthermore, the fitting results (ZARC,2 resistance values, EIS-No. 1) revealed the lowest initial resistance values for Li-PRISTINE among all four tested waiting times and tested lithium metal foil types. Tree-like structures were the dominant observed lithium deposition type throughout the full range of tested waiting times.

For **Li-TIME-AGED** (the aged over time lithium foil, which was stored for several years in an Ar-filled glovebox) the laser microscopic images revealed dominant fissure-like patterns above the lamellar pattern from the manufacturing process, which indicate a change of the surface character compared to Li-PRISTINE. Furthermore, the fitting results (ZARC,2 resistance values, EIS-No. 1) showed medium initial resistance values for Li-TIME-AGED foils among the four tested waiting times and tested lithium metal foil types. As a result, tree-like structures were observed as the predominant lithium deposition type for shorter waiting times (3 h, 8 h). For waiting times  $\geq$  24 h, spherical structures became the predominant deposition type.

For **Li-ART.-AGED**, Li-PRISTINE foils exposed to nitrogen gas  $(N_2)$  for 1 h at 25 °C in an evacuation chamber of a glove box, the laser microscopic images revealed dominant fissure-like patterns above the lamellar pattern from the manufacturing process, which indicate a change of the surface character compared to Li-PRISTINE. Furthermore, the fitting results (ZARC,2 resistance values, EIS-No. 1) showed the highest initial resistance values for Li-ART.-AGED foils among the four tested waiting times and tested lithium metal foil types. As a result, tree-like structures were observed as the predominant lithium deposition type for shorter waiting times (3 h, 8 h). For waiting times  $\geq 24 \text{ h}$ , tree-like and spherical structures became the predominant deposition type.

Most optical results of Li-ART.-AGED are between those of Li-PRISTINE and Li-TIME-AGED. This indicates, that the aging process in the glovebox might be influenced by slow chemical reactions between lithium metal and traces of nitrogen in the glovebox. The higher values for the impedance might indicate that the interphase is not yet in an equilibrium state. These results confirm our working hypothesis that nitrogen plays an important role in surface interactions on lithium metal foils with its surrounding atmosphere. From the obtained experimental results we derived the assumption that nitrogen  $(N_2)$  has an unexpected and massive influence on the deposition behavior of metallic lithium. Since nitrogen can only be detected with cost-intensive equipment and thus probably is not monitored in most gloveboxes, nitrogen is our prime suspect to explain

the variations of initial ZARC,2 resistance values (See EIS-No. 1). This finding seems to be significant for the handling of lithium metal foils.

#### **Conclusions**

In this study, an in-situ optical cell was built to investigate the behavior of lithium deposits on face-to-face orientated lithium metal electrodes. Three different lithium foils at various conditions were evaluated. The purpose of the study was to investigate the lithium deposition properties as a function of the contact time between lithium electrode (Li<sup>0</sup>) and electrolyte solution.

It is concluded that referring to lithium depositions generally as "dendrites", is too unspecific to describe the variety of possible lithium deposition morphologies. We suggest to catalogue lithium depositions obtained in optical cell setups according to their morphology, texture and color to facilitate future discussions. For each characteristic type of lithium morphology that is identified in this study, various literatures were reviewed to correlate proposed forms and nomenclatures with the corresponding morphologies. In the absence of previously reported attributes, new names are suggested. The study shows that the deposition of lithium metal on lithium metal electrodes stored under different conditions varies in terms of morphology and texture.

Four super classes and twelve subclasses of lithium morphologies were identified. Towards shorter contact periods between the lithium electrodes and the electrolyte ( $t_{wait} \leq 8$  h), compact and rough structures such as "tree-like" structures have been found as dominant morphologies. At longer contact times (e.g.  $t_{wait} \geq 24$  h), fibrous and fluffy morphologies, such as "sea ball" and "steel wool", are found to be the more dominant morphology. Laser microscopic images also indicated that the metal surfaces of Li-ART.-AGED and Li-TIME-AGED were not as smooth and free of defects when compared to the Li-PRISTINE-sample. For Li-TIME-AGED and Li-ART.-AGED foils, grain boundaries were clearly present, which indicate a change in the surface properties compared to the pristine sample. The evaluated data indicated that there is a correlation between the resistance values and (1) the time where the EIS-measurement were conducted (EIS 1, EIS 2, EIS 3, EIS 4), (2) the contact time between electrolyte and lithium electrode (WAIT 1) and (3) the type of lithium foil and aging condition (Li-PRISTINE. Li-ART.-AGED, Li-TIME-AGED).

Our working hypothesis, that nitrogen plays an important role in surface interactions on lithium metal foils with the surrounding atmosphere, could be confirmed. We derived the thesis that nitrogen  $(N_2)$  has an unexpected and massive influence on the lithium metal deposition behavior and is our prime suspect to explain the variations of initial ZARC,2 resistance values (See EIS-No. 1). During the course of the experiments it became clear that the relation between the experimental conditions (e.g. lithium foil type, preconditioning, storage, waiting time in the electrolyte) and the identified morphologies is an extremely complex parameter space. This reflects the current situation in lithium metal as well as lithium ion battery research, showing that e.g. dendrite formation is extremely difficult to predict and therefore almost impossible to avoid. The early unsuccessful attempts to commercialize lithium metal batteries by MoliEnergy have clearly shown dendrite and thus lithium morphology formations extremely difficult to control. In our current contribution we have attempted to control the experimental conditions as perfectly as possible, yet recognizing that it appears challenging to create straight relationships between waiting times, lithium type foils, storage conditions etc. and the observed morphologies. Nevertheless, our contributions are an attempt to controlled lithium deposition conditions on lithium metal surfaces as well as categorizing the identified morphologies of lithium deposition morphologies.

# Acknowledgments

We thank the BMW Group for their financial support of this study. This project has received also funding from the European Union's Horizon 2020 research and innovation program under grant agreement no. 769929. We thank Dr. Gebrekidan Gebresilassie Eshetu for the valuable discussions and proofreading.

# References

- 1. B. Liu, J.-G. Zhang, and W. Xu, *Joule*, **2**, 833–845 (2018).
- 2. J.-G. Zhang, W. Xu, and W. A. Henderson, *Lithium Metal Anodes and Rechargeable Lithium Metal Batteries*, Springer International Publishing, Cham, (2017).
- 3. E. Wiberg and N. Wiberg, *Lehrbuch der anorganischen Chemie* A. F. Holleman and G. Fischer, Editors, 102., stark umgearbeitete und verbesserte Auflage., p. 2149, Walter de Gruyter, Berlin New York, (2007).
- 4. P. W. Atkins, Ed., *Shriver & Atkins' inorganic chemistry*, 5th ed., p. 824, Oxford University Press, Oxford; New York, (2010).
- J. Meija, T. B. Coplen, M. Berglund, W. A. Brand, P. De Bièvre, M. Gröning, N. E. Holden, J. Irrgeher, R. D. Loss, T. Walczyk, and T. Prohaska, *Pure and Applied Chemistry*, 88, 265–291 (2016).
- 6. G. G. Eshetu, X. Judez, C. Li, M. Martinez-Ibañez, I. Gracia, O. Bondarchuk, J. Carrasco, L. M. Rodriguez-Martinez, H. Zhang, and M. Armand, *J. Am. Chem. Soc.*, **140**, 9921–9933 (2018).
- 7. H. Zhang, X. Judez, A. Santiago, M. Martinez-Ibañez, M. Á. Muñoz-Márquez, J. Carrasco, C. Li, G. G. Eshetu, and M. Armand, *Adv. Energy Mater.*, **9**, 1900763 (2019).
- 8. S. Tan, J. Yue, X. Hu, Z. Shen, W. Wang, J. Li, T. Zuo, H. Duan, Y. Xiao, Y. Yin, R. Wen, and Y. Guo, *Angew. Chem.*, **131**, 7884–7889 (2019).
- 9. H. Ye, Z. Zheng, H. Yao, S. Liu, T. Zuo, X. Wu, Y. Yin, N. Li, J. Gu, F. Cao, and Y. Guo, *Angew. Chem.*, **131**, 1106–1111 (2019).
- 10. D. Zhang, Y. Yin, C. Liu, and S. Fan, *Chem. Commun.*, **51**, 322–325 (2015).
- 11. D. Zhou, A. Tkacheva, X. Tang, B. Sun, D. Shanmukaraj, P. Li, F. Zhang, M. Armand, and G. Wang, *Angew. Chem. Int. Ed.*, **58**, 6001–6006 (2019).
- 12. P. Zou, Y. Wang, S.-W. Chiang, X. Wang, F. Kang, and C. Yang, *Nat Commun*, **9**, 464 (2018).
- 13. S. Wenzel, T. Leichtweiss, D. Krüger, J. Sann, and J. Janek, *Solid State Ionics*, **278**, 98–105 (2015).
- 14. S. H. Kim, K. Kim, H. Choi, D. Im, S. Heo, and H. S. Choi, *J. Mater. Chem. A*, **7**, 13650–13657 (2019).
- 15. M. Golozar, A. Paolella, H. Demers, S. Bessette, M. Lagacé, P. Bouchard, A. Guerfi, R. Gauvin, and K. Zaghib, *Commun Chem*, **2**, 131 (2019).
- 16. M. Golozar, P. Hovington, A. Paolella, S. Bessette, M. Lagacé, P. Bouchard, H. Demers, R. Gauvin, and K. Zaghib, *Nano Lett.*, **18**, 7583–7589 (2018).

- 17. P. Hovington, M. Simoneau, M. Lagacé, P. Noël, and E. Dupuis, *Microsc Microanal*, **8**, 1388–1389 (2002).
- 18. H. Ghassemi, M. Au, N. Chen, P. A. Heiden, and R. S. Yassar, *Appl. Phys. Lett.*, **99**, 123113 (2011).
- 19. X. H. Liu, L. Zhong, L. Q. Zhang, A. Kushima, S. X. Mao, J. Li, Z. Z. Ye, J. P. Sullivan, and J. Y. Huang, *Appl. Phys. Lett.*, **98**, 183107 (2011).
- 20. Y. S. Cohen, Y. Cohen, and D. Aurbach, J. Phys. Chem. B, 104, 12282–12291 (2000).
- 21. P. Bai, J. Li, F. R. Brushett, and M. Z. Bazant, *Energy Environ. Sci.*, **9**, 3221–3229 (2016).
- 22. Z. Guo, J. Zhu, J. Feng, and S. Du, RSC Adv., 5, 69514–69521 (2015).
- 23. S. J. Harris, A. Timmons, D. R. Baker, and C. Monroe, *Chemical Physics Letters*, **485**, 265–274 (2010).
- 24. P. C. Howlett, D. R. MacFarlane, and A. F. Hollenkamp, *Journal of Power Sources*, **114**, 277–284 (2003).
- 25. L. Kong, Y. Xing, and M. G. Pecht, *IEEE Access*, **6**, 8387–8393 (2018).
- 26. W. Li, H. Yao, K. Yan, G. Zheng, Z. Liang, Y.-M. Chiang, and Y. Cui, *Nat Commun*, **6**, 7436 (2015).
- 27. C. T. Love, O. A. Baturina, and K. E. Swider-Lyons, *ECS Electrochemistry Letters*, **4**, A24–A27 (2014).
- 28. T. Nishida, K. Nishikawa, M. Rosso, and Y. Fukunaka, *Electrochimica Acta*, **100**, 333–341 (2013).
- 29. M. S. Park, S. B. Ma, D. J. Lee, D. Im, S.-G. Doo, and O. Yamamoto, *Sci Rep*, **4**, 3815 (2015).
- 30. V. Roscher and K.-R. Riemschneider, in 2017 IEEE Sensors Applications Symposium (SAS),, p. 1–6, IEEE, Glassboro, NJ, USA (2017).
- 31. H. Sano, H. Sakaebe, and H. Matsumoto, *Journal of Power Sources*, **196**, 6663–6669 (2011).
- 32. J. Steiger, D. Kramer, and R. Mönig, *Journal of Power Sources*, **261**, 112–119 (2014).
- 33. K. N. Wood, E. Kazyak, A. F. Chadwick, K.-H. Chen, J.-G. Zhang, K. Thornton, and N. P. Dasgupta, *ACS Cent. Sci.*, **2**, 790–801 (2016).
- 34. H. Wu, D. Zhuo, D. Kong, and Y. Cui, *Nat Commun*, **5**, 5193 (2014).
- 35. M. Wu, Z. Wen, Y. Liu, X. Wang, and L. Huang, *Journal of Power Sources*, **196**, 8091–8097 (2011).

- 36. C. Brissot, M. Rosso, J.-N. Chazalviel, P. Baudry, and S. Lascaud, *Electrochimica Acta*, **43**, 1569–1574 (1998).
- 37. C. Brissot, M. Rosso, J.-N. Chazalviel, P. Baudry, and S. Lascaud, *Electrochimica Acta*, **43**, 1569–1574 (1998).
- 38. H. Wang, M. Matsui, H. Kuwata, H. Sonoki, Y. Matsuda, X. Shang, Y. Takeda, O. Yamamoto, and N. Imanishi, *Nat Commun*, **8**, 15106 (2017).
- 39. X.-B. Cheng and Q. Zhang, J. Mater. Chem. A, 3, 7207–7209 (2015).
- 40. L. Li, S. Li, and Y. Lu, *Chem. Commun.*, **54**, 6648–6661 (2018).
- 41. F. Ding, W. Xu, G. L. Graff, J. Zhang, M. L. Sushko, X. Chen, Y. Shao, M. H. Engelhard, Z. Nie, J. Xiao, X. Liu, P. V. Sushko, J. Liu, and J.-G. Zhang, *J. Am. Chem. Soc.*, **135**, 4450–4456 (2013).
- 42. K.-H. Chen, K. N. Wood, E. Kazyak, W. S. LePage, A. L. Davis, A. J. Sanchez, and N. P. Dasgupta, *J. Mater. Chem. A*, **5**, 11671–11681 (2017).
- 43. F. Shi, A. Pei, D. T. Boyle, J. Xie, X. Yu, X. Zhang, and Y. Cui, *Proc Natl Acad Sci USA*, **115**, 8529–8534 (2018).
- 44. C. Yang, K. Fu, Y. Zhang, E. Hitz, and L. Hu, *Adv. Mater.*, **29**, 1701169 (2017).
- 45. J. Yamaki, S. Tobishima, K. Hayashi, K. Saito, Y. Nemoto, and M. Arakawa, 9 (1998).
- 46. Y. He, X. Ren, Y. Xu, M. H. Engelhard, X. Li, J. Xiao, J. Liu, J.-G. Zhang, W. Xu, and C. Wang, *Nat. Nanotechnol.*, **14**, 1042–1047 (2019).
- 47. V. K. Khanna, *Nanosensors: physical, chemical, and biological*, p. 637, Taylor & Francis, Boca Raton, (2012).
- 48. S. Sörgel, *JEPT Journal of Electrochemistry and Plating Technology* (2018).
- 49. H. Witzenhausen, Elektrische Batteriespeichermodelle: Modellbildung, Parameteridentifikation und Modellreduktion; 1. Auflage, thesis, RWTH Aachen University (ISEA), Aachen (2017).
- 50. R. Dedryvère, L. Gireaud, S. Grugeon, S. Laruelle, J.-M. Tarascon, and D. Gonbeau, *J. Phys. Chem. B*, **109**, 15868–15875 (2005).
- 51. D. Aurbach, M. D. Levi, E. Levi, and A. Schechter, *J. Phys. Chem. B*, **101**, 2195–2206 (1997).

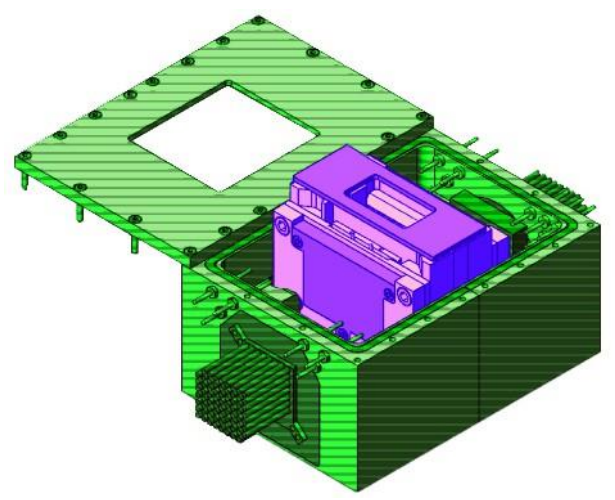


**Figure 1**. Module M1 (**green, shaded**): transport container with cable connectors, gasket and lid with optical window, Module M2 (**magenta, bright**): core unit with cuboid-shaped gasket on top of the edges of the electrolyte reservoir.

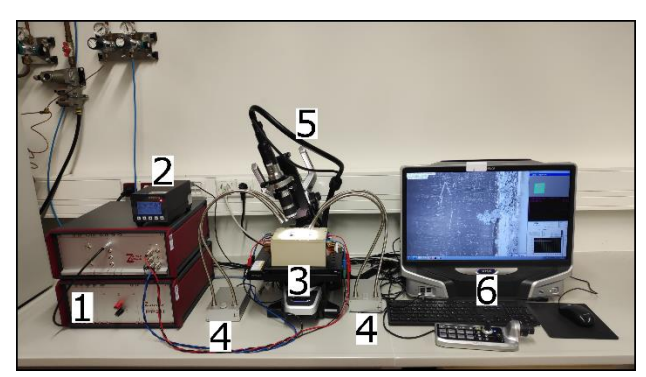


**Figure 2**. Full in situ measurement setup consisting of (1) ZAHNER potentiostat, (2), OsTECH PID-controller, (3) custom-made optical cell, (4) two HETHIS light sources, (5) KEYENCE digital microscope (6) with KEYENCE screen and console.

**TABLE I.** Electrochemical test protocols at various applied waiting times: A = 3 h, B = 8 h, C = 24 h, D = 48 h. The combination of buffer time and the corresponding waiting time WAIT 1 determined how long the lithium metal electrodes stayed in contact with the electrolyte before electrochemical experiments were conducted.

Protocol step	Time per step (s)	Image recording			
	1st Stage				
Start electrolyte filling: t <sub>zero</sub>	initial time = 0	Angles:			
Buffer time	900	0°, 5°, 20°			
One of the following (A, B, C	or D):	Magnifications:			
(A) 03h WAIT 1 phase	9,900	5x - 50x			
(B) 08h WAIT 1 phase	27,900				
(C) 24h WAIT 1 phase	85,600				
(D) 48h WAIT 1 phase	171,900				
	2 <sup>nd</sup> Stage				
EIS 1 measurement	2,220	Angle:			
CC-phase $(J = 1 \text{ mA/cm}^2)$	3,000	5°			
EIS 2 measurement	2,22				
WAIT 2 phase	3,600	Magnification:			
EIS 3 measurement	2,220	5x			
WAIT 3 phase	3,600				
EIS 4 measurement	2,220				
END	-				
	3 <sup>rd</sup> Stage				
		Angles:			
		$0^{\circ}, 5^{\circ}, 20^{\circ}$			
Further image recording					
		Magnifications:			
		5x - 50x / 50x-500x			

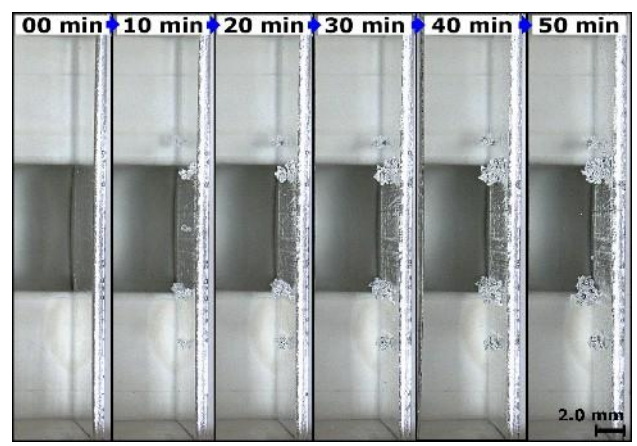


**Figure 3**. Macroscopic view through the cell's optical window of the negative lithium electrode where lithium deposition took place during the CC-phase (5°, 5x magnification).

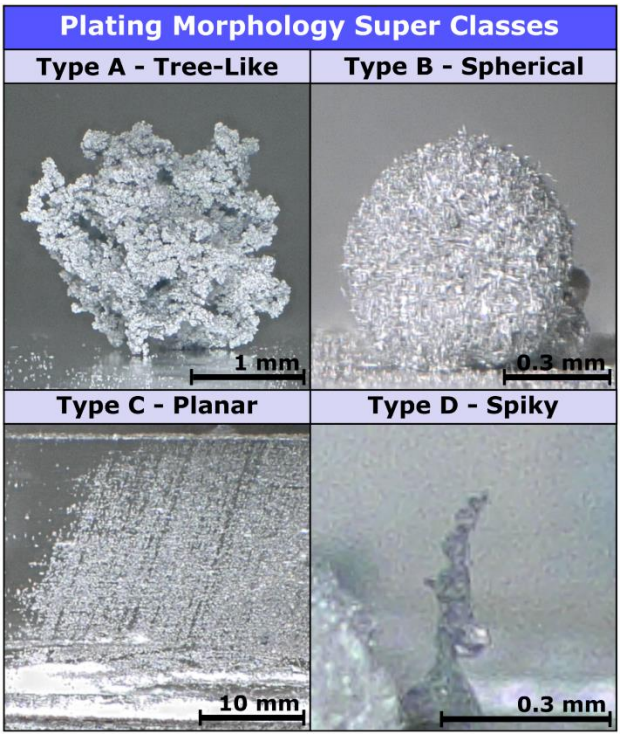


**Figure 4**. Overview of the four identified deposition super classes from the various experimental setups: A: tree-like type, B: spherical type, C: planar type, and D: spiky type.

**TABLE II.** Observed predominant lithium morphologies on the three tested lithium foil types after the defined waiting times of 3 h, 8 h, 24 h and 48 h.

Lithium foil	3hWAIT	8hWAIT	24hWAIT	48hWAIT
Li-PRISTINE	Tree-like	Tree-like	Tree-like	Tree-like
Li-ARTAGED	Tree-like	Tree-like	Tree-like & Spherical	Tree-like & Spherical
Li-TIME-AGED	Tree-like	Tree-like	Spherical	Spherical

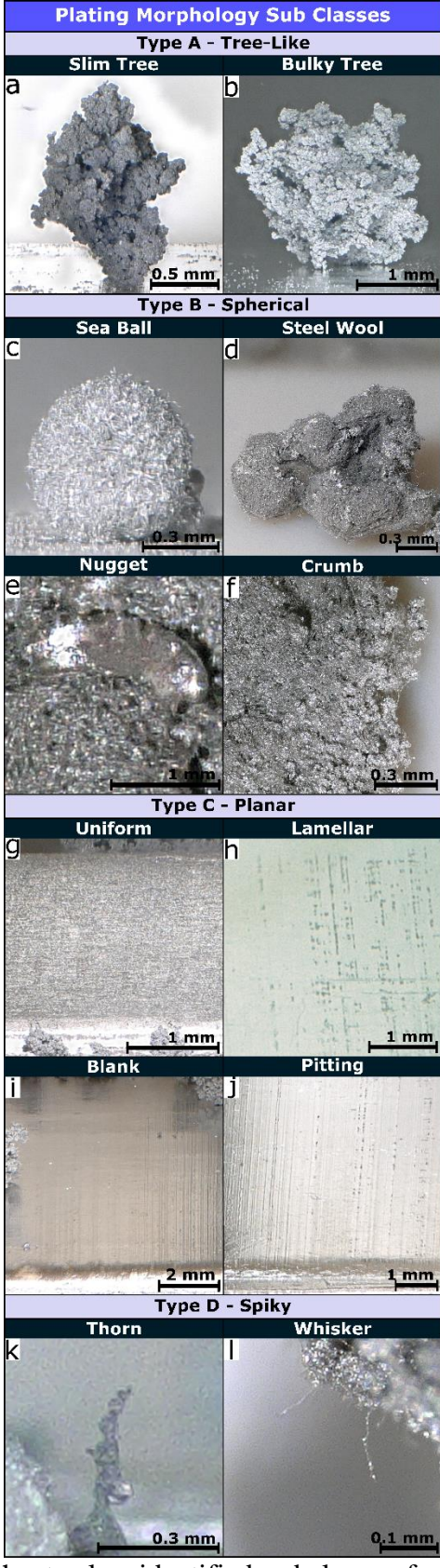


**Figure 5**. Overview of the twelve identified subclasses for morphologies of lithium depositions, which are obtained from the various electrochemical experiments.

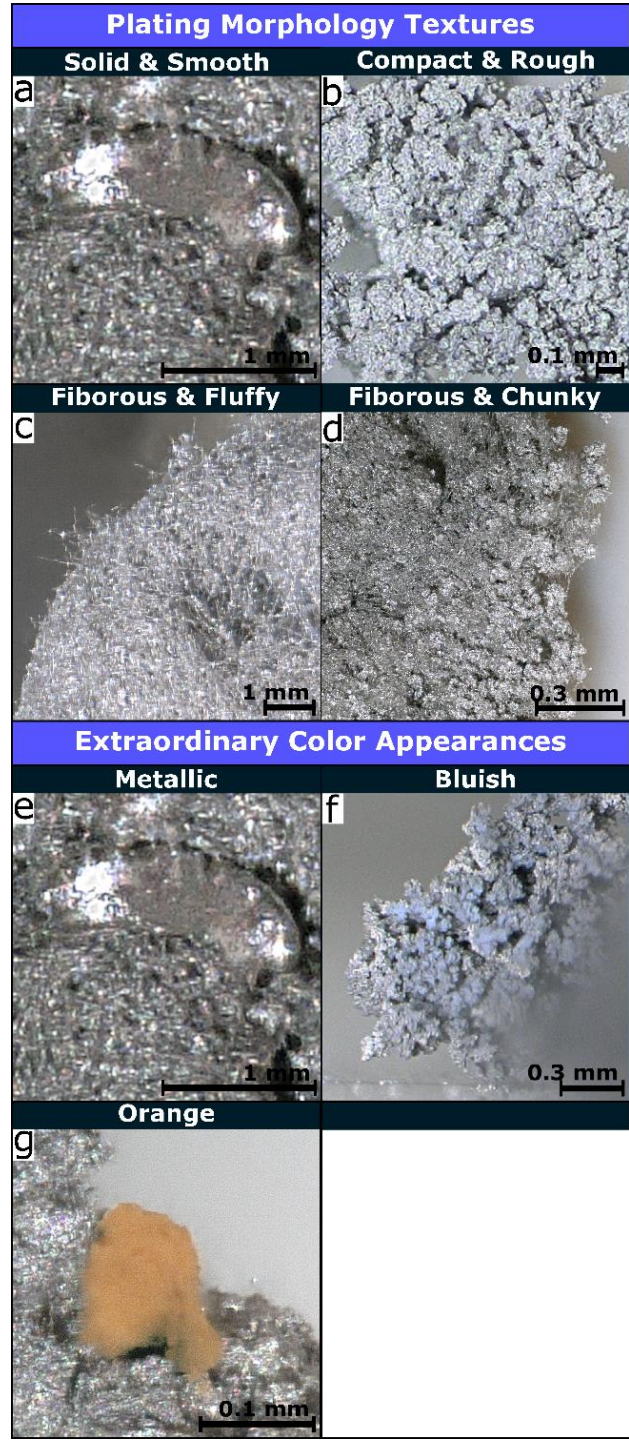


**Figure 6**. Overview of the identified textures and coloring of lithium deposition obtained from the experiments.

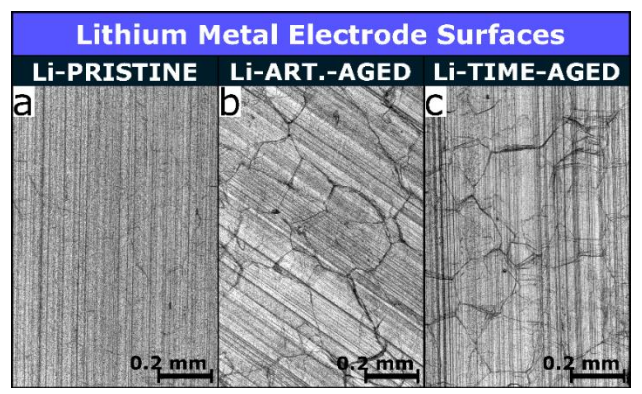


**Figure 7**. Representative laser microscope images taken from the corresponding lithium metal surfaces at 100x magnification. The three lithium foils show different surface characteristics. This could be an indication for different chemical states of the surfaces.

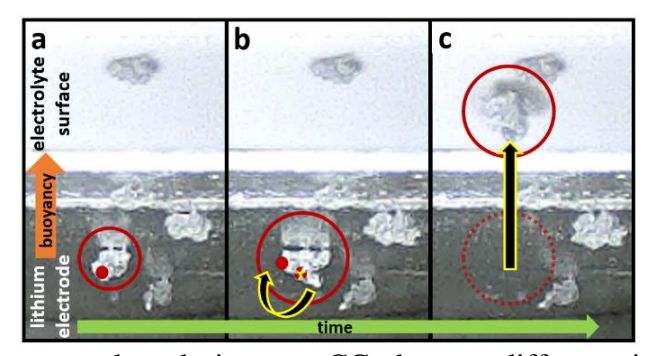


**Figure 8**. In situ images taken during one CC-phase at different time steps. A lithium crystallite growths perpendicular to the electrode surface (a). Depending on the volume and quality of the structure, it can first bend to the side (b) and then tear off and rise to the electrolyte surface (c).

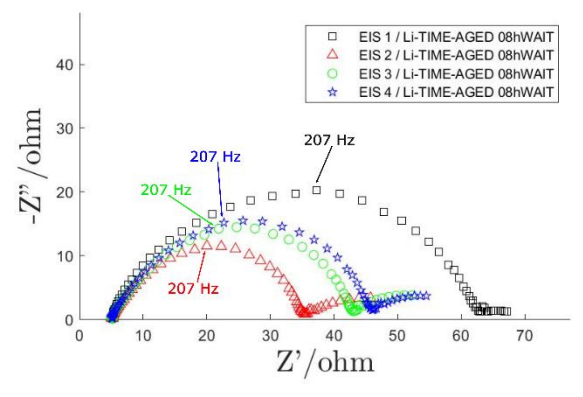


**Figure 9**. Representative Nyquist-plots for the recorded EIS-spectra (EIS 1, EIS 2, EIS 3, and EIS 4) of a single Li-TIME-AGED 8hWAIT-experiment.

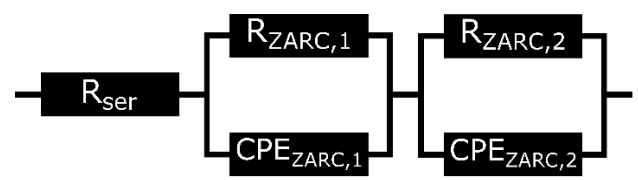
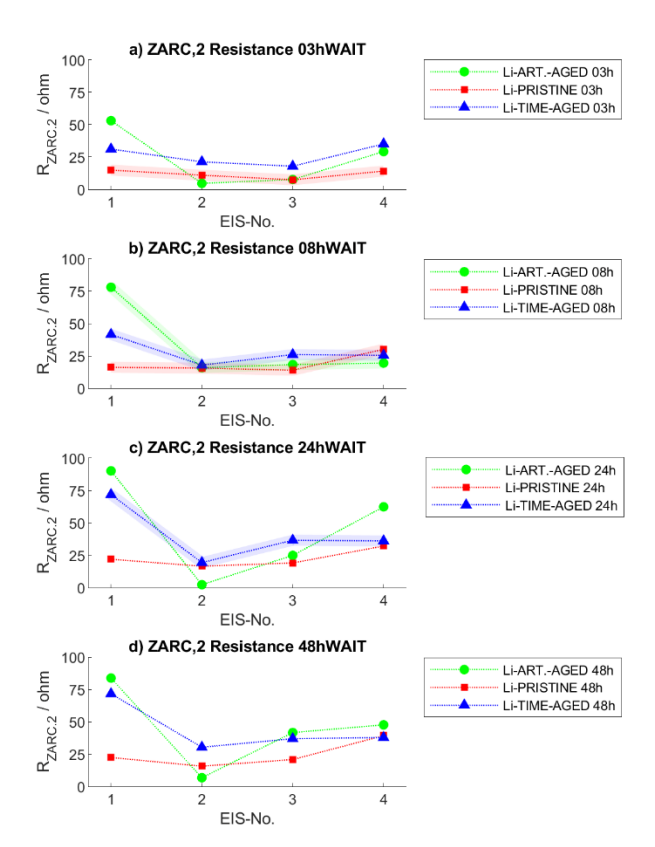


Figure 10: Electrical equivalent circuit (EEC) to model the symmetric Li<sup>0</sup>||Li<sup>0</sup> cell.



**Figure 11**. The fitted values for the resistance of the ZARC,2 element (Witzenhausen FittingGUI<sup>49</sup>). The neon shades indicate values from multiple measurements (neon shades).

**TABLE III.** Summary of the obtained data

	Li-PRISTINE	Li-ARTAGED	Li-TIME-AGED		
Treatment	Lithium in pristine	Pristine lithium foils	Lithium foils stored		
	state, as obtained	treated with N2 for	for several years in		
	from the	1 h at 25 °C	an Ar-filled		
	manufacturer		glovebox		
Predominant	Tree-like	Tree-like	Tree-like		
lithium					
morphologies (≤					
<b>24 h WAIT</b> )					
Predominant	Tree-like	Tree-like	Spherical		
lithium		& Spherical			
morphologies (≥		r			
<b>24 h WAIT</b> )					
Laser microscope	Homogeneous	Sharp and	Sharp and		
results	surface	distinctive	distinctive		
		structures on the foil	structures on the foil		
		surface	surface		
EIS results	Lowest initial	Highest initial	Medium initial		
	ZARC,2 values for	ZARC,2 values for	ZARC,2 values for		
	EIS-No. 1 values. A	EIS-No. 1 values. A	EIS-No. 1 values. A		
	rising trend with an	rising trend with an	rising trend with an		
	increasing waiting	increasing waiting	increasing waiting		
	time was observed:	time was observed:	time was observed:		
	$14.2~\Omega$ (3 h), $16.3~\Omega$	$53.0 \Omega$ (3 h), $78.0 \Omega$	$31.2~\Omega$ (3 h), $41.6~\Omega$		
	(8 h), 22.1 Ω (24 h),	$(8 \text{ h}), 90.2 \Omega$	$(8 \text{ h}), 71.9 \Omega$		
	22.6 Ω (48 h).	(24 h). Initial	(24 h), 71.7 $\Omega$		
		resistances for EIS 1	(48 h).		
		at 48 h, is located at			
		83.8 Ω.			

**TABLE IV.** ZARC,2 resistance values obtained from the curve fitting process for all setup types: Li-PRISTINE (P), Li-ART.-AGED (A) and Li-TIME-AGED (T).

EIS-No.	3hWAIT		8hWAIT		24hWAIT			48hWAIT				
	P	A	T	P	A	T	P	A	T	P	A	T
	multi	single	single	multi	multi	multi	single	single	multi	single	single	single
1	14.9	53.0	31.2	16.3	78.0	41.6	22.1	90.2	71.9	22.6	83.8	71.7
2	11.0	4.7	21.3	15.6	16.0	18.0	16.7	2.5	19.5	15.9	7.0	30.5
3	<u>7.5</u>	7.7	<u>17.9</u>	<u>14.0</u>	18.4	26.1	19.2	25.0	36.7	21.0	41.8	37.1
4	14.2	29.2	35.1	30.2	19.5	<u>25.5</u>	32.3	62.5	<u>36.2</u>	39.4	47.8	<u>37.9</u>